

PROCEEDINGS OF SPIE

SPIDigitalLibrary.org/conference-proceedings-of-spie

Hyperspectral imaging fluorescence excitation scanning spectral characteristics of remodeled mouse arteries

Joshua Deal, Stuart J. McFarland, Anna Robinson, Anna Alford, David Weber, et al.

Joshua Deal, Stuart J. McFarland, Anna Robinson, Anna Alford, David Weber, Thomas C. Rich, Silas J. Leavesley, "Hyperspectral imaging fluorescence excitation scanning spectral characteristics of remodeled mouse arteries," Proc. SPIE 10890, Label-free Biomedical Imaging and Sensing (LBIS) 2019, 108902M (4 March 2019); doi: 10.1117/12.2510770

SPIE.

Event: SPIE BiOS, 2019, San Francisco, California, United States

Hyperspectral imaging fluorescence excitation scanning spectral characteristics of remodeled mouse arteries

Joshua Deal^{1,2,3}, Stuart J. McFarland⁴, Anna Robinson⁴, Anna Alford⁵, David S. Weber⁶, Thomas C. Rich^{2,3}, Silas J. Leavesley^{1,2,3}

¹Department of Chemical & Biomolecular Engineering, University of South Alabama; ²Center for Lung Biology, University of South Alabama; ³Department of Pharmacology, University of South Alabama; ⁴College of Medicine, University of South Alabama; ⁵Department of Physics and Mathematics, Furman University; ⁶Department of Physiology & Cell Biology, University of South Alabama;

ABSTRACT

Coronary artery disease (CAD), or atherosclerosis, is responsible for nearly a third of all American deaths annually. Detection of plaques and differentiation of plaque stage remains a complicating factor for treatment. Classification of plaque before significant blockage or rupture could inform clinical decisions and prevent mortality. Current detection methods are either nonspecific, slow, or require the use of potentially harmful contrast agents. Recent advances in hyperspectral imaging could be used to detect changes in the autofluorescence of arteries associated with vessel remodeling and subsequent plaque formation and could detect and classify existing lesions. Here, we present data comparing spectral image characteristics of a mouse model designed to undergo vessel remodeling.

C57Bl/6 mice underwent ligation of three of four caudal branches of the left common carotid artery (left external carotid, internal carotid, and occipital artery) with the superior thyroid artery left intact under IACUC approved protocol. Vessels were harvested at a variety of timepoints to compare degrees of remodeling, including 4 weeks and 5 months post-surgery. Immediately following harvest, vessels were prepared by longitudinal opening to expose the luminal surface to a 20X objective. A custom inverted microscope (TE-2000, Nikon Instruments) with a Xe arc lamp and thin film tunable filter array (Versachrome, Semrock, Inc.) were used to achieve spectral imaging. Excitation scans utilized wavelengths between 340 nm and 550 nm in 5 nm increments. Hyperspectral data were generated and analyzed with custom Matlab scripts and visualized in ENVI. Preliminary data suggest consistent spectral features associated with control and remodeled vessels.

Keywords: Hyperspectral, Fluorescence, Spectroscopy, Microscopy, Signature, Linear Spectral Unmixing, Atherosclerosis, Remodel

1. INTRODUCTION

Cardiovascular disease accounts for about 1 of every 3 deaths in the United States.¹ A major component in cardiovascular disease is atherosclerosis, or hardening of the arteries due to plaque buildup inside vessels. Complications due to atherosclerosis include altered blood flow, changes in blood vessel morphology, modulation of cell adhesion molecule expression, recruitment of monocytes, and more.² These complications compound, restricting blood flow to major organs and potentially leading to rupture of a vulnerable plaque, causing immediate downstream effects such as heart attack or stroke. Several models have been used to study plaque building phenomena in animals^{3,4}, but most models ignore the effects of disturbed blood flow on atherosclerosis development. A few models make use of areas of disturbed flow by creating partial carotid ligations to lower flow and alter oscillatory shear stress in targeted areas of the vessel, shown to cause flow-dependent vascular remodeling, including intima-media-adventitial thickening.^{5,6}

Clinically, the gold standard for plaque detection and subsequent intervention is determination of percentage of stenosis via angiography. Unfortunately, stenosis percentage has been shown to correlate poorly with clinical outcomes and several other detection methods are advancing to better detect plaques and assess their risks.⁷⁻¹⁰ Among the methods for plaque detection and risk assessment are those that do not require addition of contrast material or other potentially harmful exogenous labels, but still yield data about the composition of plaques and their surrounding environment.^{11,12} The above low flow animal models combined with high-specificity spectral imaging represents a unique opportunity to

determine what, if any, molecular components are altered in vascular remodeling. To that end, we have combined the use of a new spectral imaging modality that scans the fluorescence excitation spectrum of samples to study the spectral response of remodeled mouse arteries in spectral ranges known to contain endogenous, naturally fluorescent (autofluorescent) molecules associated with vasculature. The initial results of two small pilot studies ($n=3$ and $n=3$) show that control arteries have a consistent spectral signature when compared to other controls from the same model, but that remodeled arteries have variations in the spectral signature at wavelengths known to correlate to the excitation spectra of endogenous autofluorescent molecules.^{11,13-16}

2. METHODS

2.1 Tissue specimens

All animal procedures are approved by the University of South Alabama Institution Animal Care and Use Committee and are in accordance with the NIH Guide for the Care and Use of Laboratory Animals. C57Bl/6 mice were anesthetized by intraperitoneal injection of ketamine (80 mg/kg) and xylazine (5 mg/kg). The neck region was epilated with Nair and disinfected with chlorhexidine. A midline incision was made, and the left common carotid (LCA) isolated by blunt dissection. Three of the four caudal branches of the LCA (external, internal and occipital) were ligated with 6-0 silk suture, leaving the superior thyroid artery patent. After closure of the incision, mice were provided normal rodent chow and water ad libitum. Vessels were harvested at a variety of timepoints to compare degrees of remodeling, including 5 months (first pilot study) and 4 weeks (second pilot study) post-surgery. The mice were euthanized using 0.1 ml of Fatal-Plus. The common carotid arteries were dissected out and stored in ice cold HEPES-buffered PSS (containing in mmol/L 134 NaCl, 6 KCl, 1 MgCl₂, 2 CaCl₂, 10 HEPES, 10 glucose; pH 7.40). Vessels were prepared for imaging as described previously.¹⁷ Briefly, arteries were cut longitudinally through the lumen and pinned flat (luminal side up) onto individual sylgard blocks using 14 μm micropins (tungsten wire bent at a 90°). Blocks were placed in a glass-bottom dish containing HEPES. The blocks were separated from the glass using 100 μm tungsten pins. The dish was mounted on an inverted fluorescence microscope for imaging. Each tissue imaging session included a minimum of three fields of view.

2.2 Excitation-scanning microscope setup and image acquisition

The initial pilot study utilized an inverted fluorescence microscope (TE-2000, Nikon Instruments, Melville, New York), 20X objective (Plan Apo λ 20X/0.75 ∞ /0.17 MRD00205, Nikon Instruments) and 300-W Xe arc lamp (Titan 300, Sunoptic Technologies, Jacksonville, Florida). Excitation wavelength tuning (340 nm – 550 nm in 5 nm increments, not including 385 nm) was achieved using a high-speed tiltable filter-wheel (Lambda VF-5, Sutter Instrument Company, Novato, California) containing a custom array of 5 thin-film tunable filters (TBP01-400/16, TBP01-438/16, TBP01-451/16, TBP01-503/15, and TBP01-564/14, Semrock Inc., Rochester, New York). Excitation and emission light were separated at 555 nm via a custom filter cube consisting of a long-pass emission filter (BLP02 561R-25, Semrock Inc.) and corresponding dichroic beamsplitter (FF555-Di03, Semrock Inc.). Fluorescence images were acquired using an electron-multiplied charge-coupled-device (EM-CCD) camera (Rolera EM-C², QImaging, Surrey, British Columbia).

The excitation-scanning microscope setup was altered between the pilot studies. The second pilot study utilized the same fluorescence microscope, objective, light source, and high-speed tiltable filter wheel, but the remaining optical components were changed to achieve greater acquisition speed and spectral sensitivity. The second set of 5 thin-film tunable filters (TBP01-378/16, TBP01-402/16, TBP01-449/15, TBP01-501/15, and TBP01-561/14, Semrock Inc., Rochester, New York) was selected to achieve greater sensitivity in the majority of the spectral range (360 nm – 550 nm, now including 385 nm) but sacrificed sensitivity in the lower ultraviolet (UV) wavelengths (340 nm – 355 nm). Two additional filter cubes were utilized for the second pilot study to investigate the effects of increasing the detectable fluorescence emission range. These filter cubes consisted of dichroic beamsplitters (FF458-Di02 and FF495-Di03, Semrock, Inc.) and long-pass emission filters (BLP01-458R and FF01 496/LP-25, Semrock Inc.) to separate excitation from emission light at 458 nm and 495 nm, respectively. The new excitation wavelength ranges corresponding to these filter cubes were 360 nm – 450 nm and 360 nm – 485 nm, in 5 nm increments. Fluorescence images were acquired using a high-sensitivity scientific complementary metal-oxide semiconductor (sCMOS) camera (Prime 95B, Photometrics, Tucson, Arizona). Hereafter, the filter cubes will be referred to as the wavelength where excitation and emission light separation was achieved. That is, 458 nm dichroic, 495 nm dichroic, and 555 nm dichroic.

2.3 Image Processing and Analysis

Spectral images were processed into image stacks with a custom MATLAB (MathWorks, Natick, MA) script. An image stack was constructed for each field of view (FOV) collected in the initial pilot study. Image stacks were also constructed for each spectral scan per FOV per filter cube in the second pilot study (i.e. the same FOV was captured and reconstructed as 360 - 450 nm, a 360 - 485 nm, and 360 - 550 nm excitation range images). All three-dimensional image cubes were composed of two spatial and one spectral dimension (spectral image cube). Images were RGB false-colored in the spectral dimension according to intensity values at 10%, 50%, and 90% of the available spectral range. Excitation wavelength images selected for false-coloring are listed in Table 1. False-colored images were opened in ENVI software (Exelis Visual Information Solutions, Boulder, CO) to select background regions for background spectral subtraction. Background subtraction and correction of wavelength-dependent illumination to a National Institute of Standards and Technology-traceable (NIST-traceable) lamp (LS-1-CAL-INT, Oceans Optics, Inc.) and fiber-coupled spectrometer (QE65000, Ocean Optics, Inc.) have been described previously.^{18,19} Briefly, an area containing no tissue was selected for a pixel-averaged background spectrum per specimen. Using a custom MATLAB script, this spectrum was subtracted from all fields of view for each respective specimen, then multiplied by the correction factor determined previously by use of the NIST-traceable lamp and fiber-coupled spectrometer. Corrected images were also visualized with ENVI software. Reported spectra were acquired as a pixel-averaged spectrum of the entire FOV for each spectral image stack. All extracted spectra were plotted using Excel (Office 2016, Microsoft Corporation, Albuquerque, NM). Unless otherwise stated, all spectra were normalized to a value of unity at the excitation wavelength with the strongest signal.

	"Blue Wavelength"	"Green Wavelength"	"Red Wavelength"
555 nm dichroic (pilot study 1)	355 nm	445 nm	530 nm
458 nm dichroic (pilot study 2)	365 nm	405 nm	440 nm
495 nm dichroic (pilot study 2)	370 nm	420 nm	470 nm
555 nm dichroic (pilot study 2)	375 nm	455 nm	530 nm

Table 1. Excitation wavelength images chosen for blue, green and red false-coloring and subsequent merger to achieve an RGB-visualization of excitation hyperspectral image stacks.

3. RESULTS AND DISCUSSION

Arteries contain several molecules known to be autofluorescent.^{13,20,21} Principal among the molecules necessary for arterial structure are collagen and elastin. Both elastin and various types of collagen are found within the internal elastic lamina, the layer immediately below the endothelial cell lining of the arteries, as well as throughout the remaining sections of the artery: the media, external elastic lamina, and adventitia.²²⁻²⁴ The presence of these fibrous proteins is easily seen with traditional histological staining methods.²⁵ Furthermore, from the inside out, these layers are 0.2 to 0.5 μm thick (endothelium), $\sim 0.1 \mu\text{m}$ thick (internal elastic lamina), 25 μm to 1mm thick (media), 0.1 to 0.2 μm thick (external elastic lamina), with a variable adventitial thickness, thinned in these experiments by trimming of connective tissue for the purposes of these studies.²²⁻²⁴ Given the small diameter of the vessels (mouse carotid arteries have a vessel diameter of no more than 0.7 μm ²⁶) and a rule of thumb of 50 μm media thickness per 1 mm vessel diameter,²² even a 340 nm excitation wavelength should penetrate through the vessel into the adventitial layer.²⁷ Shown in Figure 1, the primary autofluorescent component appears to be elastin from the elastic lamina layers, as evidenced by the presence of wavy white lines, with white indicating that the wavy lines have relatively high signal across the breadth of the excitation scanning range. (i.e. detectable signal in the images false colored blue, green, and red merged to create the RGB composite image.) Images shown in Figure 1 are representative of every excitation scan taken of each artery, in that wavy white lines are the hallmark of an arterial excitation-scanning hyperspectral image stack.

Additionally, several products of cellular respiration, namely nicotinamide adenine dinucleotide (NADH) and flavin adenine dinucleotide (FAD) are present throughout these cell layers and known to be autofluorescent.^{13,20} Furthermore, some components of blood, such as porphyrins, and molecules recruited during remodeling and atherosclerosis, such as lipofuscins, have been shown to be both autofluorescent and present in arteries.^{13,20} As the longest reported peak excitation wavelength of each molecule listed is shorter than 550 nm, variations in any of these previously listed molecules could cause deviations in the spectral signature of arteries in the ranges considered in this study. Figure 2

shows representative FOVs of both control (Figure 2 A,B) and remodeled (Figure 2 C,D) arteries, as well as the average spectral signature per sample (Figure 2E). Initial results indicate a relatively conserved spectral signature for the control vessels while the spectra of the remodeled arteries have variations in the UV range (340-360 nm), less relative intensity from wavelengths near the beginning of the visual spectrum (360-420 nm), and more relative intensity beyond 500 nm.

Following the first pilot study, several upgrades to the spectral imaging microscope were made, including a filter set with higher sensitivity in a large subset the original spectral scanning range and a sCMOS camera with increased acquisition speed and much higher sensitivity than the previous EM-CCD camera. Additionally, several literature reviews and pilot studies on the spectra of autofluorescent molecules elucidated regions of these spectra that may vary due to disease states or remodeling.^{11-16,20,21} These studies revealed that most autofluorescent molecules have peak excitation wavelengths at or below 450 nm. The following data come from a second pilot study where we investigated the effects of choosing filter cubes with wavelength cutoffs at shorter wavelengths, namely 458 nm and 495 nm, on both image and spectral data. The visual differences of false-colored images per choice of dichroic filter cube are shown in Figure 3.

Visually, the false-colored images from the 555 nm dichroic in Figure 3 give a much more comprehensive picture of the data, in that various spectral features are easier to discern as different colors in the false-colored image. The false-colored control artery image from the 458 nm dichroic is almost entirely red, indicating that most of the visual data is contained primarily in the 440 nm image. The 495 nm dichroic image from the same vessel looks largely similar to the 458 nm dichroic image with a more orange tint, indicating that the same data displayed in the 458 nm dichroic image also contains significant intensity data at the 420 nm and 470 nm wavelengths. The excitation range available for the 555 nm dichroic is broad enough to begin to distinguish the bluish structure in the FOV as mostly UV while also filling in an area with the 530 nm image that appeared to be empty space when using the other two dichroic filter cubes. However, while the 555 nm dichroic image for the remodeled artery also outlines reddish structures not previously obvious when using the other two dichroic filter cubes, the same image also illustrates the weakness of using the 555 nm dichroic. As most of the autofluorescent molecules have peak excitation wavelengths at or below 450 nm, the emission data is significantly weaker at the 555 nm collection point. The lack of abundant fluorescence emission reduces the ability to separate signal from background. This difficulty of separation resulted in reduced signal-to-noise ratio, visualized below as a hazier image, particularly in the remodeled image. To illustrate the differences in detectable signal when using the different dichroic filter cubes, Figure 4 shows the raw intensities for the images in Figure 3 after background subtraction and spectral output correction.

As shown in Figure 4, the signal intensity when using the 555 nm dichroic is significantly lower than with the other two dichroic filter cubes. However, an interesting phenomenon is seen within the 380 – 400 nm range; the raw intensity for the 458 nm dichroic drops below that of the 495 nm dichroic and remains there for the rest of the scanning range. This shift in intensity is present in every subject, regardless of control or remodeled sample. Because several autofluorescent molecules have peak excitation wavelengths in the UV range and Stokes shift are generally relatively short, the 495 nm and 555 nm dichroics collect very little of the emitted light from samples excited in those UV ranges. This results in a much more robust detectable signal in the UV excitation portion of the spectrum when using the 458 nm dichroic as opposed to the other two dichroics. The 495 nm dichroic notably begins to provide more detectable signal than the 458 nm dichroic about 40 nm into the scanning range. That is, the reversal of prominent signal sensitivity occurs at approximately the distance between the two cutoff points for signal collection determined by the dichroic filter cubes. Regardless, the 555 nm dichroic likely has a cutoff wavelength far beyond the peak emission wavelengths of most autofluorescent molecules, resulting in appreciably less available signal than with the other two dichroic filter cubes. Hence, careful consideration should be taken to choose a meaningful wavelength range, as a tradeoff in intensity of available signal could be worthwhile if the acquired data elucidates differences not easily detectable in a shorter excitation scanning range (Figure 3).

Although the visual data from the 555 nm dichroic (Figure 3) appear compelling, examination of both raw intensity and normalized intensity data from the 555 nm dichroic (Figure 5) reveal few to no meaningful trends. Two of the three remodeled arteries (animals 1 and 3) were observed to have significantly higher raw detectable signal than their control counterparts. The signal intensities were much closer in value in the remaining artery pair (animal 2). Beyond these observations, the normalized intensity data show almost no discernable spectral differences in control and remodeled arteries. However, normalized intensity data collected using the 458 nm and 495 nm dichroic filter cubes reveal a more consistent spectral signature of control arteries, with the notable exception of the control artery for the first

animal (Figure 6). The data from this artery appears to be an outlier, likely due to user error during either data collection or processing (Figure 7).

Figure 7 shows that the spectral image data from mouse 1 are unlike any other data from the remainder of the experiment. The images collected contain blue, amorphous regions that do not appear to correlate to any structure. These amorphous regions are likely either noise resulting from improper background subtraction or a contaminant in the sample which has altered the spectral data obtained from these images. Selection of a subset of the image for spectral data collection (i.e. regions of interest selected to be devoid of blue, amorphous regions) shows a spectrum more similar to the control artery data from the other two mice. However, data from the selected regions are still significantly different from the other two control arteries. This could indicate that the interfering signal was too high in magnitude to overcome by compensation with specific region selection alone or that the mouse 1 control artery was a genuine outlier. Computation of averages and standard deviations from a much more robust data set could determine which, if either of these scenarios, is the case.

4. CONCLUSIONS AND FUTURE WORK

Atherosclerosis remains a multi-faceted, difficult, and deadly disease that affects a significant portion of developed countries. Many detection methodologies fail to detect underlying structural changes and further fail to accurately predict the likelihood of severe complications such as heart attack or stroke. Excitation-scanning hyperspectral imaging has the power to discern structural changes in arteries which may be precursors to these events and may elucidate both an accurate risk and a best treatment option. The first pilot study included animals with up to 5 months of remodeling due to oscillatory flow. The spectral data from these animals showed little variation in spectral data among control arteries without altered flow patterns and large regions of the excitation spectra where the spectral signature varied in the remodeled arteries. Experimentation with and literature reviews of the excitation spectra of autofluorescent molecules inspired a second pilot study to investigate the effects of variable scanning and detection ranges of autofluorescent signals from these arteries remodeled by exposure to oscillatory flow. Preliminary data suggests that shorter scanning and longer detection ranges provide additional information with increased signal sensitivity, but with the cost of omitting changes in signal outside of those scanning ranges.

The changes in spectral signature from the data shown here correlate well with autofluorescent molecule peak excitation spectra reported in literature, as well as spectral signatures of some of these molecules that we have reported previously. Furthermore, the molecules in question have been reported to play large-scale roles in initial vessel remodeling and subsequent atherosclerosis. However, the data shown here come from small pilot studies ($n=3$). Expanding the pilot study to contain significantly more data points will likely establish a more definite spectral signature of control arteries and reveal excitation wavelength ranges with common deviations in excitation spectra of remodeled vessels. Furthermore, similarity among data presented here has been subjectively determined through visualization of image and spectral data. Future studies will expand the available data pool with a larger number of samples and employ a defined metric for what constitutes significance among spectral deviations.

5. ACKNOWLEDGEMENTS

We would like to acknowledge the Abraham Mitchell Cancer Research fund as well as the American Heart Association grant 18PRE34060163, National Science Foundation grant NSF 1725937, and National Institutes of Health grants P01HL066299, UL1 TR001417, S10RR027535, and S10OD020149 for supporting this work. Drs. Leavesley and Rich also disclose financial interest in a start-up company, SpectraCyte LLC, formed to commercialize spectral imaging technologies.

REFERENCES

- [1] MEMBERS, W.G., Benjamin, E.J., Blaha, M.J., Chiuve, S.E., Cushman, M., Das, S.R., Deo, R., de Ferranti, S.D., Floyd, J., et al., “Heart disease and stroke statistics—2017 update: a report from the American Heart Association,” *Circulation* 135(10), e146 (2017).
- [2] Simionescu, M., and Sima, A.V., [Morphology of Atherosclerotic Lesions] , in *Inflamm. Atheroscler.*, G. Wick and C. Grundtman, Eds., Springer Vienna, Vienna, 19–37 (2012).
- [3] Getz, G.S., and Reardon, C.A., “Animal Models of Atherosclerosis,” *Arteriosclerosis, Thrombosis, and Vascular Biology* 32(5), 1104–1115 (2012).
- [4] Hofker, M.H., van Vlijmen, B.J., and Havekes, L.M., “Transgenic mouse models to study the role of APOE in hyperlipidemia and atherosclerosis,” *Atherosclerosis* 137(1), 1–11 (1998).
- [5] Nam, D., Ni, C.-W., Rezvan, A., Suo, J., Budzyn, K., Llanos, A., Harrison, D., Giddens, D., and Jo, H., “Partial carotid ligation is a model of acutely induced disturbed flow, leading to rapid endothelial dysfunction and atherosclerosis,” *American Journal of Physiology-Heart and Circulatory Physiology* 297(4), H1535 (2009).
- [6] Korshunov, V.A., and Berk, B.C., “Flow-induced vascular remodeling in the mouse: a model for carotid intima-media thickening,” *Arteriosclerosis, thrombosis, and vascular biology* 23(12), 2185–2191 (2003).
- [7] Warlow, C., Sudlow, C., Dennis, M., Wardlaw, J., and Sandercock, P., “Stroke (vol 362, pg 1211, 2003),” *LANCET* 363(9406), 402–402 (2004).
- [8] Weinberger, J., “Diagnosis and prevention of atherosclerotic cerebral infarction,” *CNS spectrums* 10(7), 553–566 (2005).
- [9] Hingwala, D., Kesavadas, C., Sylaja, P.N., Thomas, B., and Kapilamoorthy, T.R., “Multimodality imaging of carotid atherosclerotic plaque: Going beyond stenosis,” *The Indian journal of radiology & imaging* 23(1), 26 (2013).
- [10] Matter, C.M., Stuber, M., and Nahrendorf, M., “Imaging of the unstable plaque: how far have we got?,” *European Heart Journal* 30(21), 2566–2574 (2009).
- [11] Uchida, Y., Uchida, Y., Kawai, S., Kanamaru, R., Sugiyama, Y., Tomaru, T., Maezawa, Y., and Kameda, N., “Detection of Vulnerable Coronary Plaques by Color Fluorescent Angioscopy,” *JACC: Cardiovascular Imaging* 3(4), 398–408 (2010).
- [12] Uchida, Y., and Maezawa, Y., [Molecular imaging of atherosclerotic coronary plaques by fluorescent angioscopy] , INTECH Open Access Publisher (2012).
- [13] Ramanujam, N., “Fluorescence spectroscopy of neoplastic and non-neoplastic tissues,” *Neoplasia* 2(1–2), 89–117 (2000).
- [14] Korneva, Y.S., Dorosevich, A.E., and Maryakhina, V.S., “Fluorescent diagnostics of epithelial neoplasms of different colon parts,” *Lasers in surgery and medicine* 49(8), 763–766 (2017).
- [15] Korneva, Y.S., Dorosevich, A., and Maryakhina, V., “Investigation of malignant transformation of sporadic adenomas of colon by fluorimetry,” *Lasers in medical science* 32(2), 363–367 (2017).
- [16] Nebuloni, M., Albarello, L., Andolfo, A., Magagnotti, C., Genovese, L., Locatelli, I., Tonon, G., Longhi, E., Zerbi, P., et al., “Insight on colorectal carcinoma infiltration by studying perilesional extracellular matrix,” *Scientific reports* 6, 22522 (2016).
- [17] Francis, M., Waldrup, J., Qian, X., and Taylor, M.S., “Automated analysis of dynamic Ca² signals in image sequences,” *J Vis Exp* (2014).
- [18] Leavesley, S.J., Annamdevula, N., Boni, J., Stocker, S., Grant, K., Troyanovsky, B., Rich, T.C., and Alvarez, D.F., “Hyperspectral imaging microscopy for identification and quantitative analysis of fluorescently-labeled cells in highly autofluorescent tissue,” *Journal of Biophotonics* 5(1), 67–84 (2012).
- [19] Annamdevula, N.S., Sweat, B., Favreau, P., Lindsey, A.S., Alvarez, D.F., Rich, T.C., and Leavesley, S.J., “An approach for characterizing and comparing hyperspectral microscopy systems,” *Sensors* 13(7), 9267–9293 (2013).
- [20] Croce, A., and Bottiroli, G., “Autofluorescence spectroscopy and imaging: a tool for biomedical research and diagnosis,” *European journal of histochemistry: EJH* 58(4), (2014).
- [21] Gillies, R., Zonios, G., Anderson, R.R., and Kollias, N., “Fluorescence excitation spectroscopy provides information about human skin in vivo,” *Journal of Investigative Dermatology* 115(4), 704–707 (2000).
- [22] “BME 332: Blood Vessel Structure-Function,” <<http://www.umich.edu/~bme332/chap11bloodvessel/bme332bloodves.htm>> (17 December 2018).
- [23] Fung, Y., [Biomechanics: mechanical properties of living tissues] , Springer Science & Business Media (2013).
- [24] King, M.W., [Integrative medical biochemistry: examination and board review/Michael W. King.] , New York: McGraw-Hill Education Medical, (2014).

- [25] Sindram, D., Martin, K., Meadows, J.P., Prabhu, A.S., Heath, J.J., McKillop, I.H., and Iannitti, D.A., "Collagen-elastin ratio predicts burst pressure of arterial seals created using a bipolar vessel sealing device in a porcine model," *Surgical endoscopy* 25(8), 2604–2612 (2011).
- [26] Amin, M., Le, V.P., and Wagenseil, J.E., "Mechanical testing of mouse carotid arteries: from newborn to adult," *Journal of visualized experiments: JoVE*(60), (2012).
- [27] Avci, P., Gupta, A., Sadasivam, M., Vecchio, D., Pam, Z., Pam, N., and Hamblin, M.R., "Low-level laser (light) therapy (LLLT) in skin: stimulating, healing, restoring," presented at *Seminars in cutaneous medicine and surgery*, 2013, 41.

FIGURES

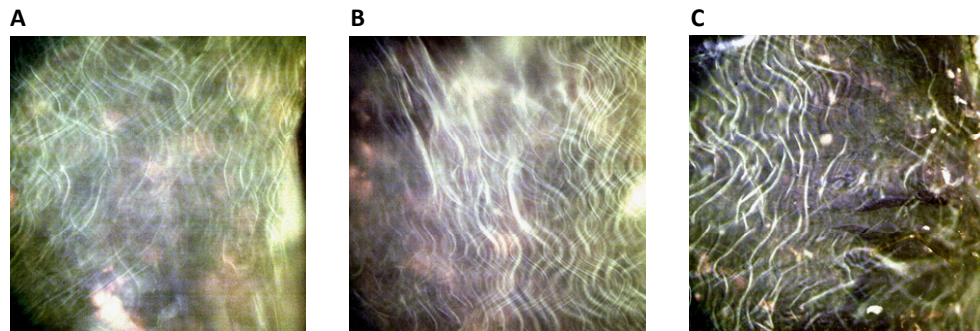


Figure 1. Representative hyperspectral images of control mouse carotid arteries. Images were given an RGB false-coloring by merging the excitation images at 355 nm, 445 nm, and 530 nm with a blue, green, and red false coloring, respectively. A) The greenish hue of the image suggests signal concentrated more closely to the middle of the excitation spectral scanning range (445 nm) than the fringes (355 nm and 530 nm). The wavy white lines of the elastin in the elastic lamina are clearly visible. B) A second field of view from the same artery as (A). The apparent layering of wavy white lines might indicate detection of both the internal and external elastic lamina. C) A field of view from a different control mouse artery. In particular, this field of view contains punctate white areas not visible in the other two images. These punctate regions could be sections of the elastin that run vertically through the sample but are likely an altogether different component, as the lamina forms a ring around the vessel which should translate to a thin sheet when pinned flat. As with the presumed elastin, the white coloration implies relatively strong signal in each false-colored channel.

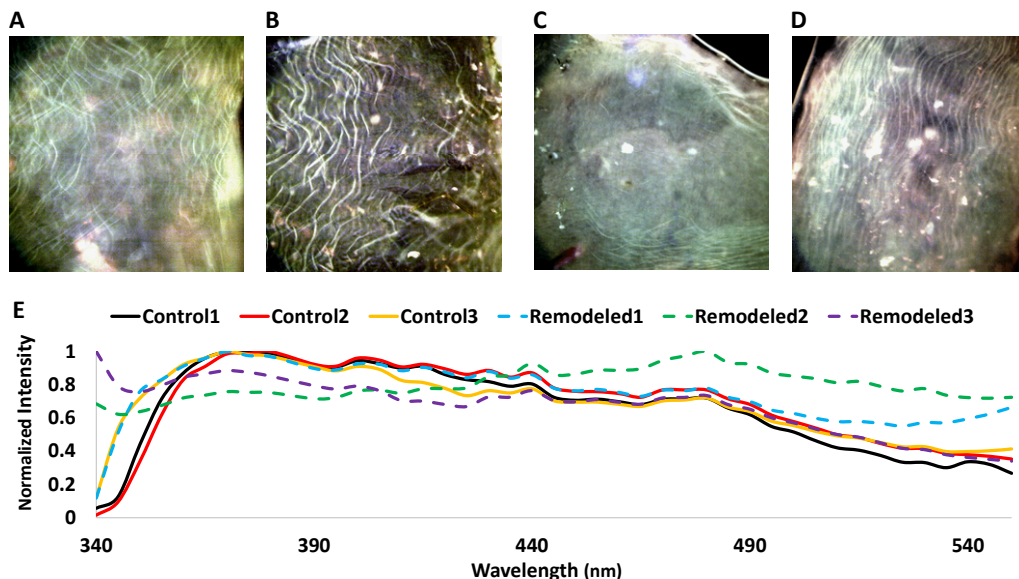


Figure 2. Comparison of control versus remodeled arteries. Images were false-colored in the same manner as Figure 1. A,B) False-colored images of control mouse carotid arteries. C,D) False-colored images of remodeled mouse carotid arteries. E) Average excitation spectra of control (solid lines) and remodeled (dashed lines) mouse arteries. Average spectra were computed as the mean of the pixel-averaged spectrum of the entire field of view of each image per specimen. All spectra were normalized to a value of unity at the wavelength with the strongest signal.

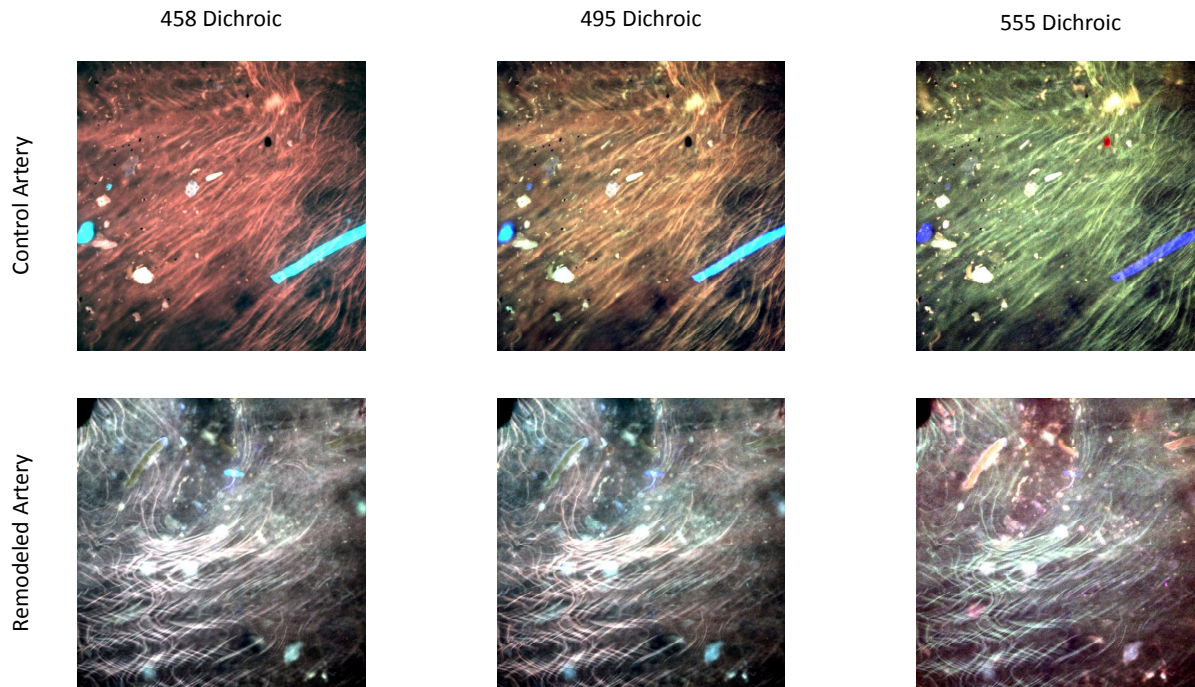


Figure 3. False-colored images of control (top row) and remodeled (bottom row) arteries per image stack acquired using the 458 nm (left), 495 nm (center) and 555 nm (right) dichroic filter cubes. The 458 nm dichroic included an excitation scanning range of 360 – 450 nm. RGB false-coloring was achieved by merging the images at 365 nm, 405 nm, and 440 nm false colored blue, green, and red, respectively. The 495 nm dichroic included an excitation scanning range of 360 – 485 nm. RGB false-coloring was achieved by merging the images at 370 nm, 420 nm, and 470 nm false colored blue, green, and red, respectively. The 555 nm dichroic included an excitation scanning range of 360 – 550 nm. RGB false-coloring was achieved by merging the images at 375 nm, 455 nm, and 530 nm false colored blue, green, and red, respectively.

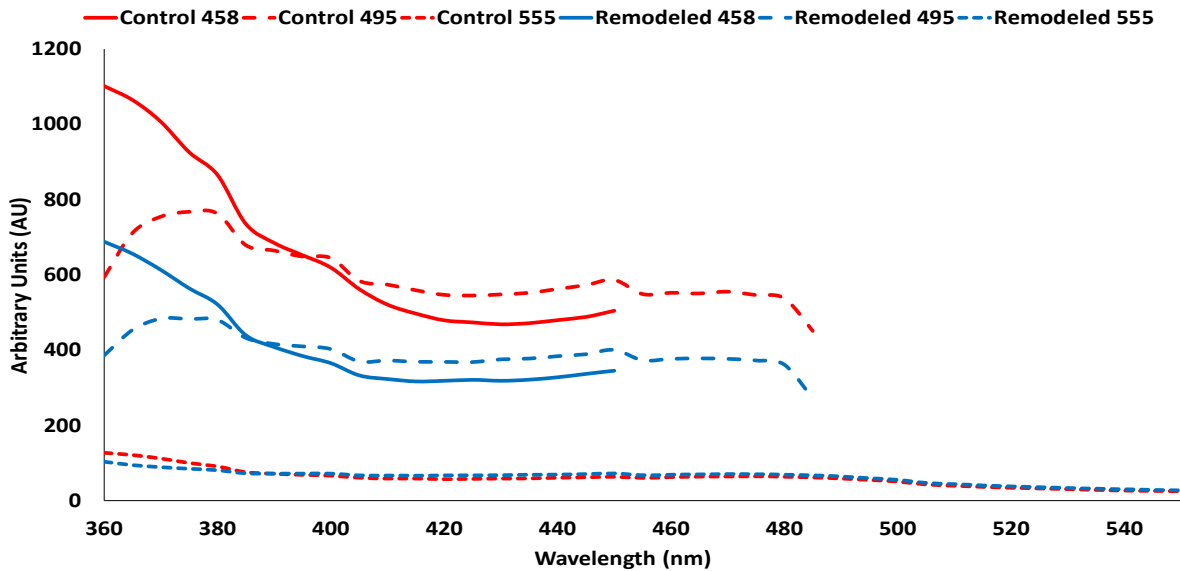


Figure 4. Raw intensity data of images presented in Figure 3 after background subtraction and correction factor multiplication. Data from the control and remodeled arteries are represented by red and blue lines, respectively. Data from the 458 nm, 495 nm, and 555 nm dichroics are represented by solid lines, long dashes, and short dashes, respectively. Intensities measured using the 458 and 495 dichroics are comparable, while intensities measured using the 555 nm dichroic are much lower, indicating reduced signal strength.

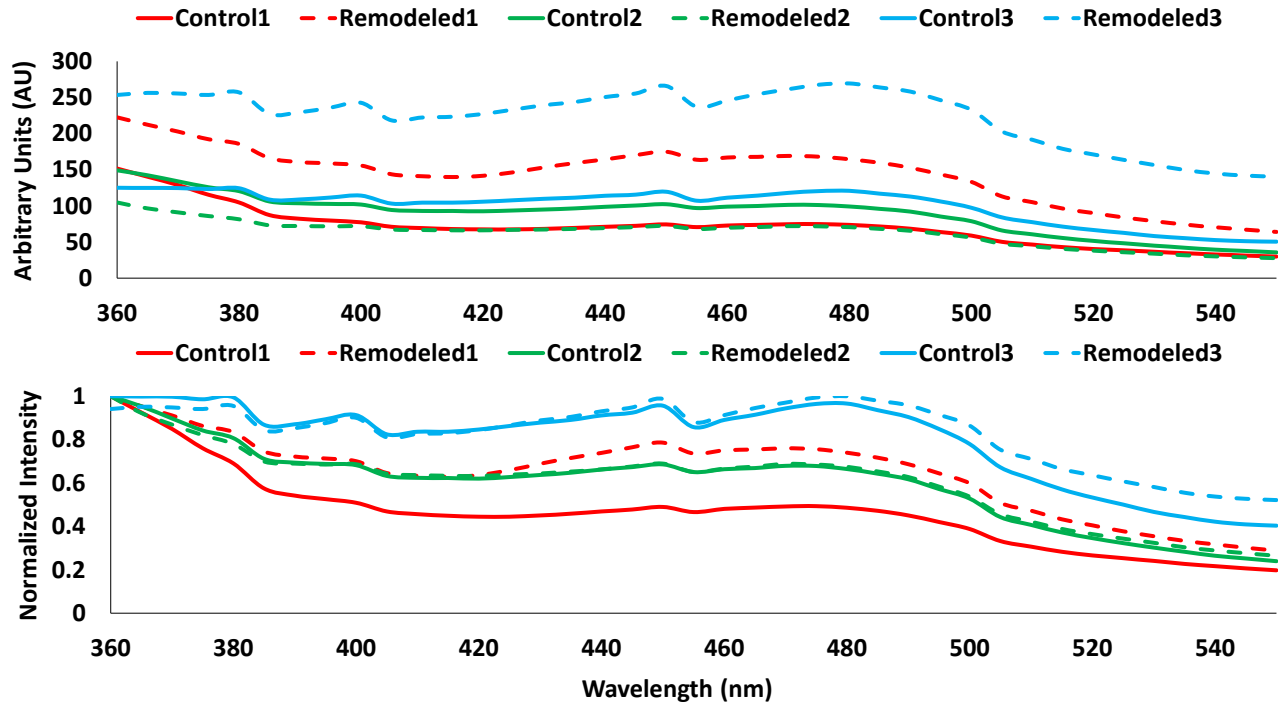


Figure 5. Raw intensity (top) and normalized intensity (bottom) data acquired with the 555 nm dichroic averaged per animal for every animal in the second pilot study. Control artery data are indicated by solid lines. Remodeled artery data are indicated by dashed lines. Animals 1, 2, and 3 are represented as red, green, and blue lines, respectively.

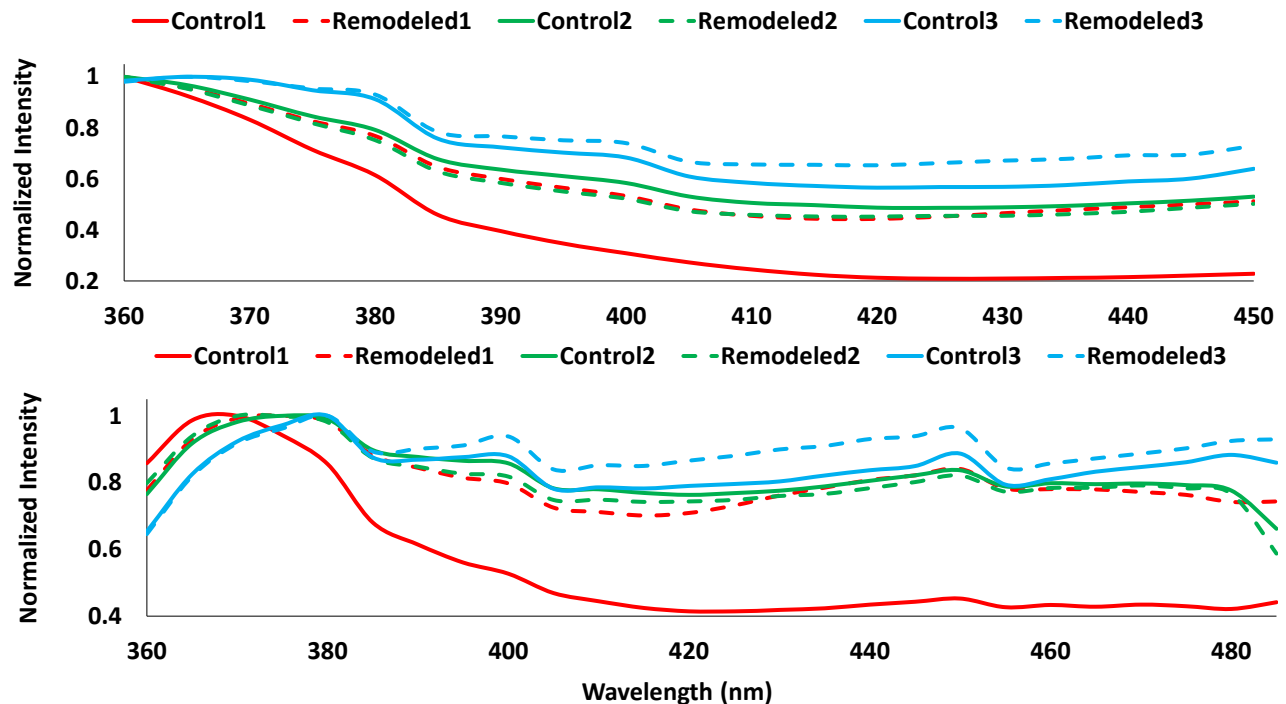


Figure 6. Normalized intensity acquired with the 458 nm (top) and 495 nm (bottom) dichroics averaged per animal for every animal in the second pilot study. Control artery data are indicated by solid lines. Remodeled artery data are indicated by dashed lines. Animals 1, 2, and 3 are represented as red, green, and blue lines, respectively.

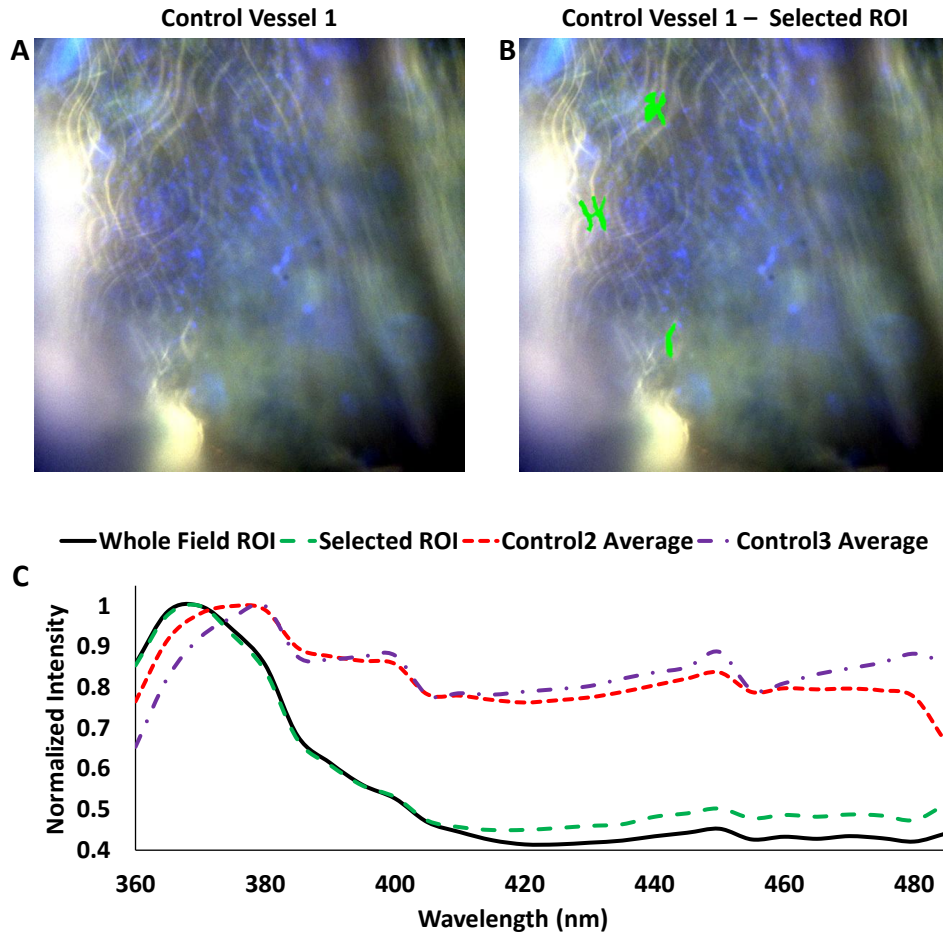


Figure 7. Image and spectral data acquired using the 495 nm dichroic for the control artery of mouse 1. (A) The original RGB false-colored image. The entirety of this image was selected as the region of interest to obtain spectral data. (B) The RGB false-colored image with selected (green) regions to obtain a subset of the spectral data. (C) Comparison of spectral data from the entirety of the field of view (black solid line) to the selected regions (green long dashed line) and the other two control arteries in the study. Control 2 average is shown as a red short dashed line and the control 3 average is shown as a purple dot dashed line.